ACS APPLIED MATERIALS & INTERFACES

www.acsami.org

Research Article

Synergistic Transition-Metal Selenide Heterostructure as a High-Performance Cathode for Rechargeable Aluminum Batteries

Tianming Liu, Guocheng Lv,* Meng Liu, Changchun Zhao,* Libing Liao, Hao Liu, Jiayan Shi, Jian Zhang, and Juchen Guo*

Cite This: *ACS Appl. Mater. Interfaces* 2023, 15, 11906−11913

Read Online

ACCESS | Metrics & More | Article Recommendations | Supporting Information

ABSTRACT: We synthesize and characterize a rechargeable aluminum battery cathode material composed of heterostructured Co_3Se_4/ZnSe embedded in a hollow carbon matrix. This heterostructure is synthesized from a metal−organic framework composite, in which ZIF-8 is grown on the surface of ZIF-67 cube. Both experimental and theoretical studies indicate that the internal electric field across the heterostructure interface between Co_3Se_4 and ZnSe promotes the fast transport of electron and Al-ion diffusion. As a result, the heterostructured Co_3Se_4/ZnSe demonstrates superior specific capacity and cycle stability compared to the single-phase Co_3Se_4 and ZnSe cathode materials.

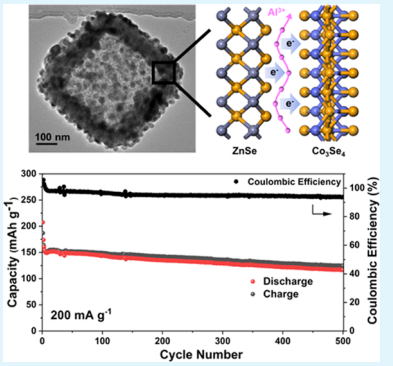

KEYWORDS: *MOF-on-MOF, heterostructure, metal selenides, Co_3Se_4/ZnSe, DFT, Al-ion battery*

INTRODUCTION

Rechargeable aluminum batteries (RABs) are a prospective large-scale energy storage technology owing to their potential low-cost and excellent safety.[1−6] However, due to the complex charge transfer mechanisms, the development of cathode materials for RABs is still at the early stage.[7−11] With the exception of Chevel Phase molybdenum sulfide (Mo_6S_8),[12−15] most transition-metal chalcogenides (TMCs) are considered conversion-type electrodes for RABs.[16−23] The conversion electrodes often undergo microstructure transformation and phase separation during cycling, which leads to the gradual deterioration of the charge transfer kinetics.[24−26] Previous studies suggest that creating a heterostructure between two semiconductors can generate an internal electric field, which promotes the directional transfer of charges.[27−29] This concept of heterostructure has been adopted to develop electrode materials for lithium, sodium, and potassium ion battery systems,[30−34] where the internal electric field in the heterostructure can improve the electrochemical reaction kinetics and ion diffusion.[35−38]

Here, we demonstrate a design of heterostructured TMC cathode materials for RABs. We synthesized cobalt selenide/zinc selenide-carbon (Co_3Se_4/ZnSe@C) hollow nanocubes from a metal−organic framework (MOF) heterostructure composed of epitaxially grown ZIF-8 on ZIF-67. We hypothesize that the internal electric field generated at the Co_3Se_4/ZnSe interface can facilitate the transport of electrons and Al^{3+} ion diffusion. Furthermore, the hollow carbon framework of the heterostructure derived from the MOF-on-MOF precursor can further promote structural stability and electrical conductivity. The synthesized Co_3Se_4/ZnSe@C nanocubes demonstrate a capacity of 276 mA h g^{-1} at 100 mA g^{-1} in the first discharge. The long-cycle capacity retention is 117 mA h g^{-1} after 500 cycles under a current density of 200 mA g^{-1}, showing good electrochemical performance. This work provides an important design principle to develop high specific capacity and cycle stability cathode materials for RABs.

EXPERIMENTAL METHODS

Synthesis of ZIF-67 and ZIF-8. ZIF-67 was prepared by the surfactant control method. In a typical synthesis, 0.58 g of $Co(NO_3)_2 \cdot 6H_2O$ and 0.01 g of cetrimonium bromide (CTAB) were added to 20 mL DI water and stirred for 15 min. The solution was added into 140 mL aqueous solution containing 9.08 g of 2-methylimidazole (2-MeIM) and stirred for 30 min at room temperature. After 24 h, the solid content from the reaction was separated with centrifugation and dried at 60 °C overnight. In a typical synthesis of ZIF-8, 6.7 g of 2-MeIM and 0.0048 g of CTAB were first dissolved in 30 mL of DI water. Then, 30 mL DI water solution of 1.8 g of $Zn(CH_3COO)_2 \cdot 2H_2O$ was added and aged for 2 h. The mixture was centrifuged and

Received: December 30, 2022
Accepted: February 10, 2023
Published: February 27, 2023

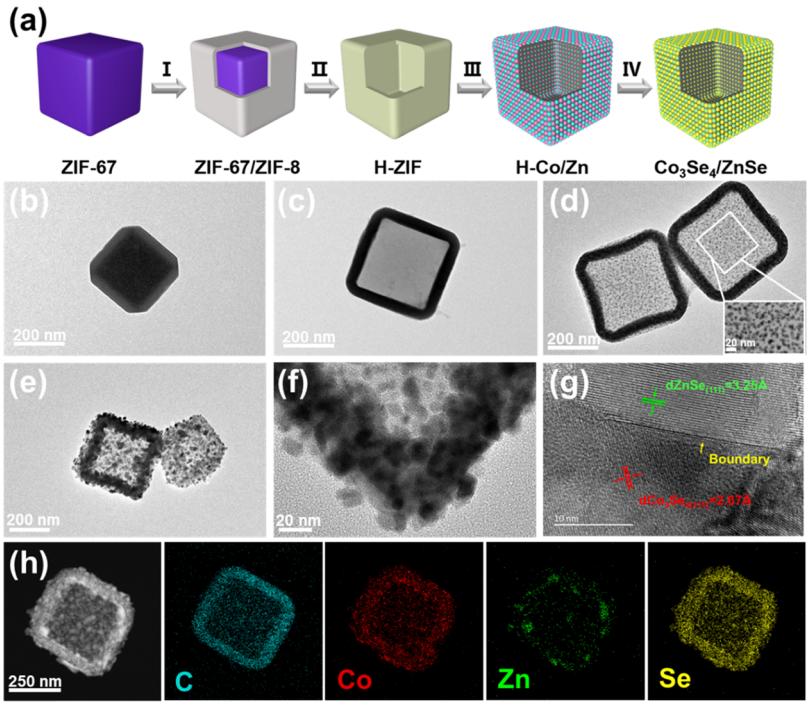

Figure 1. (a) Schematic illustration of the synthesis of Co_3Se_4/ZnSe@C nanocubes. Step I: ZIF-8 coating on ZIF-67, Step II: Etching ZIF-67/ZIF-8 by tannic acid, Step III: carbonization in Ar to form H-Co/Zn, Step IV: selenization to form Co_3Se_4/ZnSe heterostructure. TEM images of (b) ZIF-67/ZIF-8, (c) H-ZIF, and (d) H-Co/Zn. (e, f) TEM and HRTEM images of Co_3Se_4/ZnSe@C. (g) HRTEM image of lattice spacing and interface boundary of the Co_3Se_4/ZnSe heterostructure. (h) TEM elemental mapping images of all elements contained.

washed with DI water and ethanol for several times to obtain the white solid product, which is dried overnight at 60 °C.

Synthesis of ZIF-67/ZIF-8. Three hundred milligrams of the as-prepared ZIF-67 powders were dispersed in 50 mL ethanol with ultrasonication. Then, 100 mL DI water containing 200 mg of 2-MeIM was added to the ZIF-67 purple suspension. Finally, 50 mg of zinc nitrate ($Zn(NO_3)_2$) and 10 mg of CTAB were dissolved into 10 mL DI water, which was added into the suspension, and stirred for 6 h. ZIF-67/ZIF-8 was obtained after centrifugal separation and dried overnight.

Synthesis of Hollow ZIF-67/ZIF-8 (H-ZIF). The as-prepared ZIF-67/ZIF-8 powder was dispersed in 50 mL alcohol. Then, 300 mL of ethanol and DI water mixture ($V_{H_2O}/V_{ethanol}$ = 1:1) containing 300 mg of tannic acid (TA) was added and stirred for 30 min. The brown solid was centrifuged, rinsed several times with DI water and alcohol, and finally dried overnight.

Synthesis of Hollow Co/Zn (H-Co/Zn). The as-prepared H-ZIF powder was annealed at 200 °C for 0.5 h and 600 °C for 2 h with a ramp rate of 5 °C min^{-1} under argon environment. The pure hollow Co nanocubes and hollow Zn nanocubes were synthesized under similar condition using ZIF-76 and ZIF-8 precursors, respectively.

Synthesis of Co_3Se_4/ZnSe@C. The as-prepared H-Co/Zn and selenium powder are mixed at a mass ratio of 1:0.5 and heated at 650 °C for 2 h with a ramp rate of 5 °C min^{-1} under argon environment. Similarly, H-Co and H-Zn were heated with selenium to form Co_3Se_4@C and ZnSe@C.

Material Characterization. The crystal structure is characterized by X-ray diffraction (XRD; Bruker D8 focus Advance diffractometer with Cu Kα radiation (λ = 1.5406 Å), 40 kV/40 mA). The surface chemical analysis was performed with an X-ray photoelectron spectrometer (XPS; ThermoFischer, ESCALAB 250XI). All XPS spectra are corrected with C 1s at 284.80 eV. The morphology and structure of the materials were examined by a field emission scanning electron microscope (FESEM; SU-8010) and a transmission electron microscope (TEM; JEM). Thermogravimetric analysis (TGA) was performed under airflow at 10 °C min^{-1} using a TA Discovery thermal analyzer.

Electrochemical Measurements. All RABs tests were carried out with Swagelok cells using Al foil anode, one layer of glass fiber as separator, and the mixture of aluminum chloride and 1-ethyl-3-methylimidazolium chloride ($AlCl_3$-[EMIm]Cl, molar ratio = 1.3:1) ionic liquid as electrolyte. All components were dried in a vacuum oven to remove water. The prepared active material, carbon black, and polystyrene (as binder) were mixed in *N*-methyl-2-pyrotanone with a mass ratio of 6:3:1. The obtained slurry was coated on a Mo foil current collector, and dried overnight in vacuum at 60 °C. The Swagelok cells with an inner diameter of 12 mm were assembled in a glove box filled with argon, and 100 μl electrolyte was added to fully wet the separator. The galvanostatic charge−discharge tests were performed on a LAND CT2001A battery test system from 1.85 to 0.1 V. Cyclic voltammetry (CV) was performed with an electrochemical workstation (CHI 760E).

Theoretical Calculations. On the basis of density functional theory, all calculations are performed for the optimization of configuration atoms. The exchange-correlation potential is established on the generalized gradient approximation (GGA) of the Perdew−Burke−Ernzerhof (PBE) formula. The electron is considered self-consistent when the energy change is less than 10^{-6} eV. The cutoff energy is 350 eV, and the energy difference is less than 0.01 eV. The geometry optimization is considered convergent when the energy change is less than 0.03 eV $Å^{-1}$. The 3 × 3 × 1 Monkhorst−Pack grid *k*-points were used to integrate total energy in the Brillouin zone.

RESULTS AND DISCUSSION

Figure 1a illustrates the preparation process of the hollow-Co_3Se_4/ZnSe@C nanocubes. ZIF-67 nanocubes (Figure S1) were first synthesized, followed by epitaxially growing ZIF-8 on the ZIF-67 surface to form a core−shell structure (Figures 1b and S2). Hollow-ZIF-67/ZIF-8 (H-ZIF) nanocubes (Figures 1c and S3) were generated using tannic acid as the etching agent.[39,40] The obtained H-ZIF nanocubes were heat treated under an inert environment to form Co/Zn@C nanocubes composed of Co/Zn metal nanoparticles (approximately 10

https://doi.org/10.1021/acsami.2c23205
ACS Appl. Mater. Interfaces 2023, 15, 11906−11913

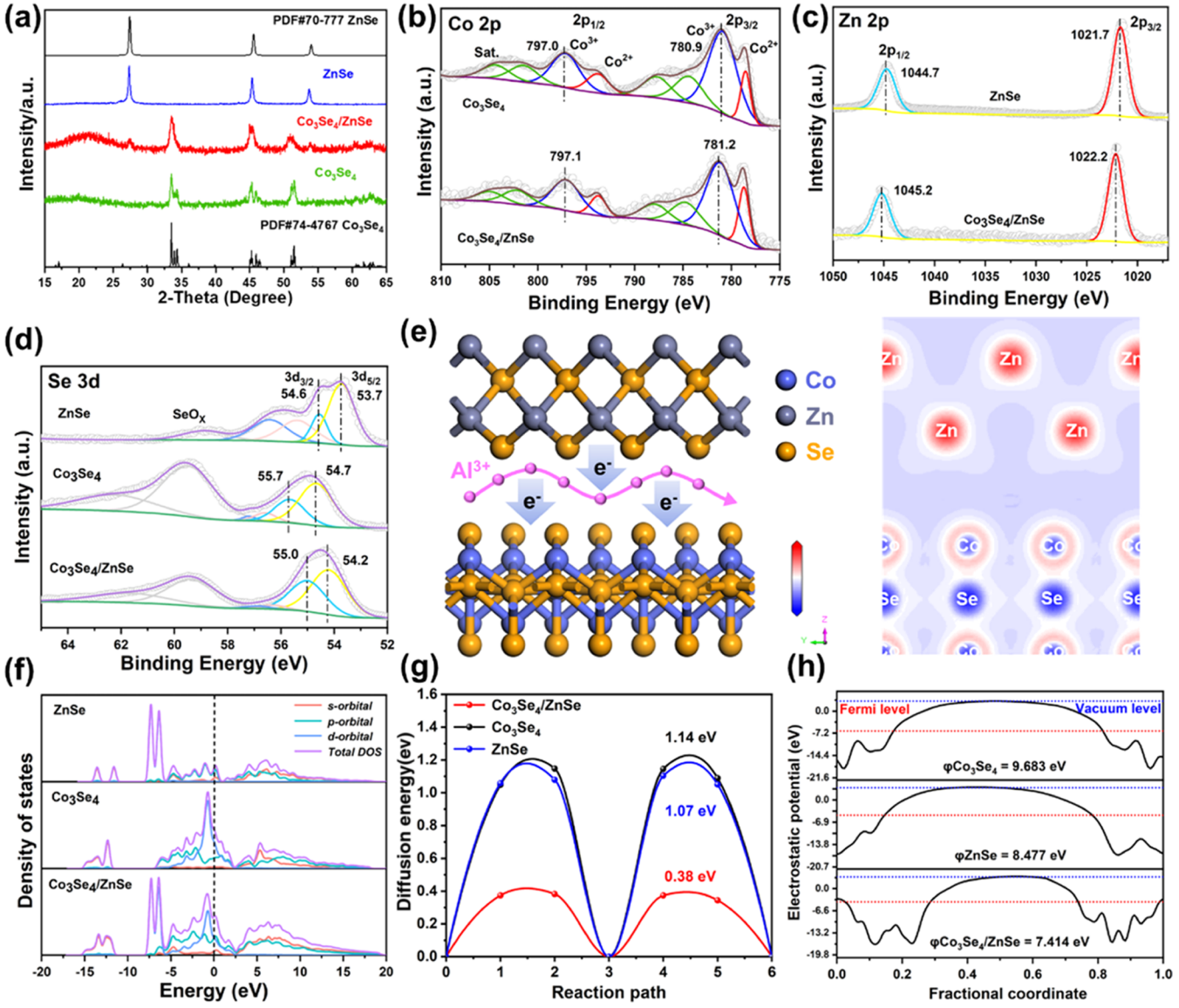

Figure 2. (a) XRD patterns of Co_3Se_4/ZnSe@C, Co_3Se_4@C, and ZnSe@C. XPS spectra of (b) Co 2p, (c) Zn 2p, and (d) Se 3d. (e) Schematic diagram of the Co_3Se_4/ZnSe heterostructure interface and contour map of charge density on the corresponding planes. (f) Calculated density of states (DOS) of the surfaces of Co_3Se_4 and ZnSe and Co_3Se_4/ZnSe interface. (g) Al migration energy barriers and (h) energy distribution curves of Co_3Se_4/ZnSe, Co_3Se_4, and ZnSe.

nm) embedded in hollow carbon shell (Figures 1d and S4). Tannic acid functioned as both carbon precursor and reducing agent in the heat treatment to enable the uniform formation of Co/Zn nanoparticles. Selenization was achieved by heating the mixture of hollow-Co/Zn@C nanocubes and selenium powder under argon at 650 °C. The Co_3Se_4/ZnSe heterostructure was induced by the Kirkendall effect in the obtained Co_3Se_4/ZnSe@C nanocubes due to different diffusion rate of Co and Zn.[41,42] The transmission electron microscopy (TEM) images of the Co_3Se_4/ZnSe@C nanocubes at different magnifications (Figure 1e,f) clearly reveal uniformly dispersed Co_3Se_4/ZnSe nanoparticles (approximately 20 nm) and the heterostructure interface between Co_3Se_4 and ZnSe. A representative heterostructure between ZnSe (111) plane (3.25 Å) and Co_3Se_4 (111) plane (2.67 Å) is shown in Figure 1g. Elemental mapping (Figure 1h) demonstrates that the elements of C, Co, Zn, and Se are uniformly distributed in the hollow nanocubes.

The X-ray diffraction (XRD) pattern of Co_3Se_4/ZnSe@C nanocubes in Figure 2a confirms that the heterostructured TMC is composed of crystalline Co_3Se_4 (JCPDS: 74-4767) and ZnSe (JCPDS: 70-777). The valence states of Co, Zn, and Se in Co_3Se_4/ZnSe@C are analyzed and compared to those in the single-selenide Co_3Se_4@C and ZnSe@C nanocubes derived from ZIF-67 and ZIF-8 using the identical procedure (TEM images in Figure S5). Figure S6 shows the carbon content in Co3Se4/ZnSe@C, Co_3Se_4@C, and ZnSe@C analyzed by TGA. As shown in Figure 2b, X-ray photoelectron spectroscopy (XPS) detected two valence states of Co from the Co_3Se_4/ZnSe heterostructure based on Co 2p spectra: Co^{3+} state indexed by the peaks located at 797.1 and 781.2 eV and Co^{2+} state at 793.8 and 778.7 eV. The Co 2p XPS spectra also indicate that the Co valence state in the Co_3Se_4/ZnSe@C heterostructure is identical to that in the single-phase Co_3Se_4@C composite. On the other hand, the Zn 2p XPS peaks from Co_3Se_4/ZnSe@C (Zn $2p_{1/2}$ located at 1045.2 eV, Zn $2p_{3/2}$

https://doi.org/10.1021/acsami.2c23205
ACS Appl. Mater. Interfaces 2023, 15, 11906−11913

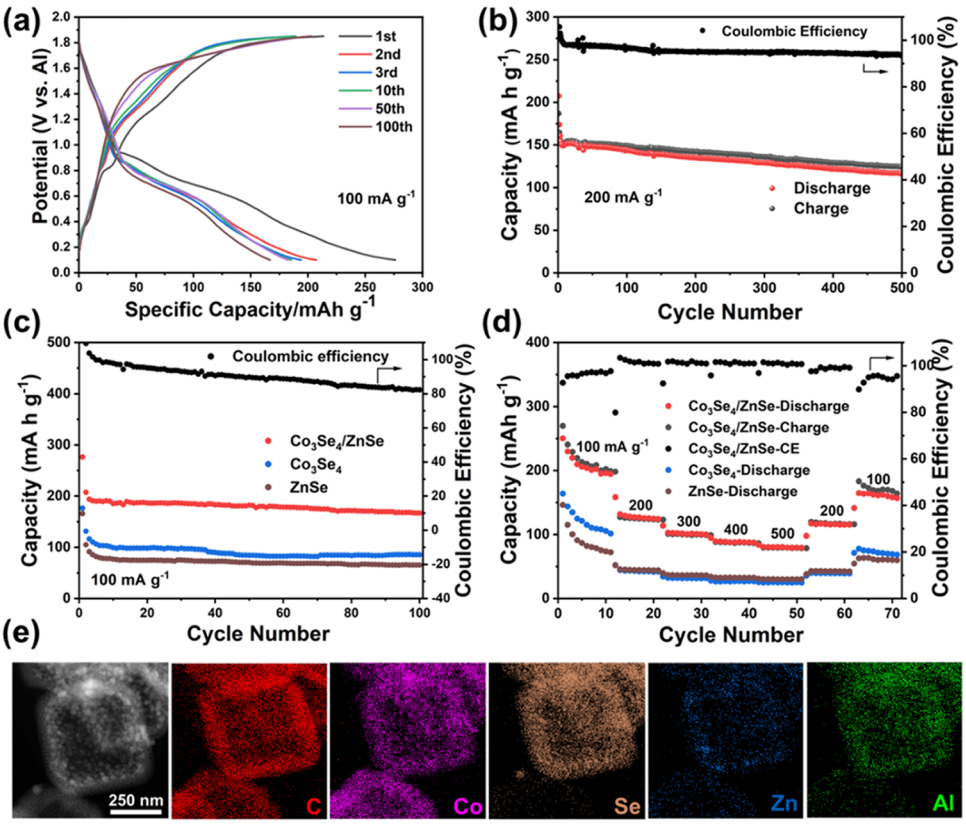

Figure 3. (a) Galvanostatic discharge−charge curves of Co_3Se_4/ZnSe@C at 100 mA g^{-1} for different cycles. (b) Long cycling performance of Co_3Se_4/ZnSe@C at 200 mA g^{-1}. (c) Cycling performance at 100 mA g^{-1} of Co_3Se_4/ZnSe@C, Co_3Se_4@C, and ZnSe@C. (d) Rate performance of Co_3Se_4/ZnSe@C, Co_3Se_4@C, and ZnSe@C ranges from 100 to 500 mA g^{-1}. (e) TEM elemental mapping images of Co_3Se_4/ZnSe@C electrode after 100 cycles at a current density of 100 mA g^{-1}.

located at 1022.2 eV) in Figure 2c demonstrate a 0.5 eV positive shift compared with the single ZnSe@C composite (Zn $2p_{1/2}$ located at 1044.7 eV, Zn $2p_{3/2}$ located at 1021.7eV). This increase in binding energy indicates the lower electron density of the Zn^{2+} cation in the Co_3Se_4/ZnSe@C heterostructure.[43−45] The Se 3d XPS spectra in Figure 2d show that the valence state of Se in the Co_3Se_4/ZnSe@C heterostructure is clearly different from that in pure Co_3Se_4@C and ZnSe@C. The valence state of Se in Co_3Se_4/ZnSe@C indicates the redistribution of interface charge in the heterostructure induced by the lattice distortion between Co_3Se_4 and ZnSe. The heterostructure properties of the Co_3Se_4/ZnSe interface were calculated based on density functional theory (DFT). Figure 2e displays the Co_3Se_4/ZnSe heterostructure model and the schematic diagram of the migration path of Al^{3+} ions and electrons. The contour diagram of the charge density on the corresponding plane proves that there is an internal electric field across the Co_3Se_4/ZnSe heterostructure interface, which promotes the directional transport of electrons (red and blue represent positive charge accumulation and negative charge loss, respectively). In Figure 2f, the calculated density of states (DOS) indicates that the Co_3Se_4/ZnSe heterostructure interface causes band bending, and the energy of the d-orbital is enhanced at the Fermi level, showing a metallic state. The calculated Al diffusion barrier in Co_3Se_4/ZnSe is 0.38 eV, significantly less than 1.14 eV in Co_3Se_4 and 1.07 eV in ZnSe (Figure 2g), which proves the faster Al diffusion at the heterostructure interface. Furthermore, to compare the minimum energy barrier of electron transfer in different phases, we calculated the work function (E_w) of Co_3Se_4/ZnSe, Co_3Se_4, and ZnSe according to eq 1,[46] the corresponding energy distribution curves are shown in Figure 2h, in which the blue and red dotted lines represent the vacuum energy level (E_{vac}) and Fermi level (E_f), respectively.

$$E_w = E_{vac} - E_f \quad (1)$$

The lowest work function energy of Co_3Se_4/ZnSe (7.414 eV) indicates the fastest electron transport at the heterostructure interface. The E_w value of Co_3Se_4 (9.683 eV) is higher than that of ZnSe (8.477 eV), demonstrating that electrons can be transferred from ZnSe to Co_3Se_4 at the interface, which establishes the internal electric field inside the heterostructure. Collectively, the DFT calculation indicates that the enhanced electron transport by the heterostructure interface of Co_3Se_4/ZnSe can significantly accelerate the kinetics of the Al^{3+} reaction.

The performance of the Co_3Se_4/ZnSe@C cathode for RABs is evaluated by the galvanostatic charge−discharge method. The discharge−charge curves of Co_3Se_4/ZnSe@C (Figure 3a) demonstrate a discharge platform at 0.9 V and a charge platform at 1.2 V with 276 mA h g^{-1} first discharge capacity and 214 mA h g^{-1} first charge capacity at 100 mA g^{-1}. The higher discharge capacity may be attributed to the dissolution of the Al_2O_3 layer on the Al anode and the formation of solid electrolyte interphase (SEI).[47,48] The consistent charge−discharge curves at different cycles indicate excellent cycle stability of Co_3Se_4/ZnSe@C. Figure 3b shows the long-term cycling performance of the Co_3Se_4/ZnSe@C cathode at 200 mA g^{-1}. The first discharge capacity is 207 mA h g^{-1}, and it is

https://doi.org/10.1021/acsami.2c23205
ACS Appl. Mater. Interfaces 2023, 15, 11906−11913

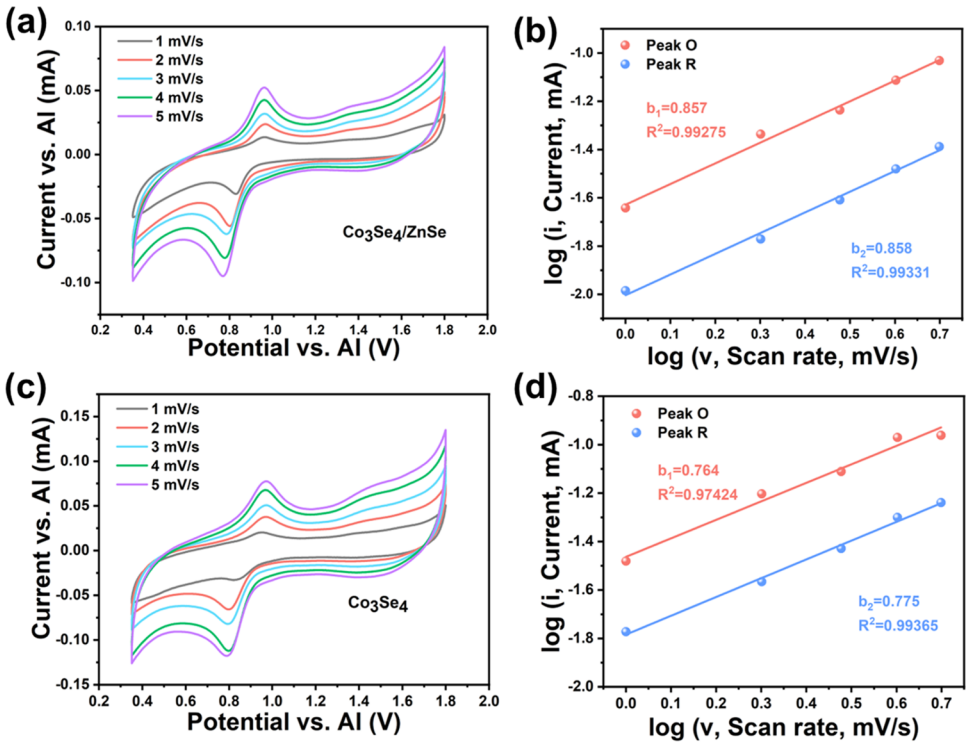

Figure 4. (a, c) CV curves of Co_3Se_4/ZnSe@C and Co_3Se_4@C electrode at different scan rate from 1 to 5 mV s^{-1} and (b, d) the corresponding log (i) versus log (v) plots.

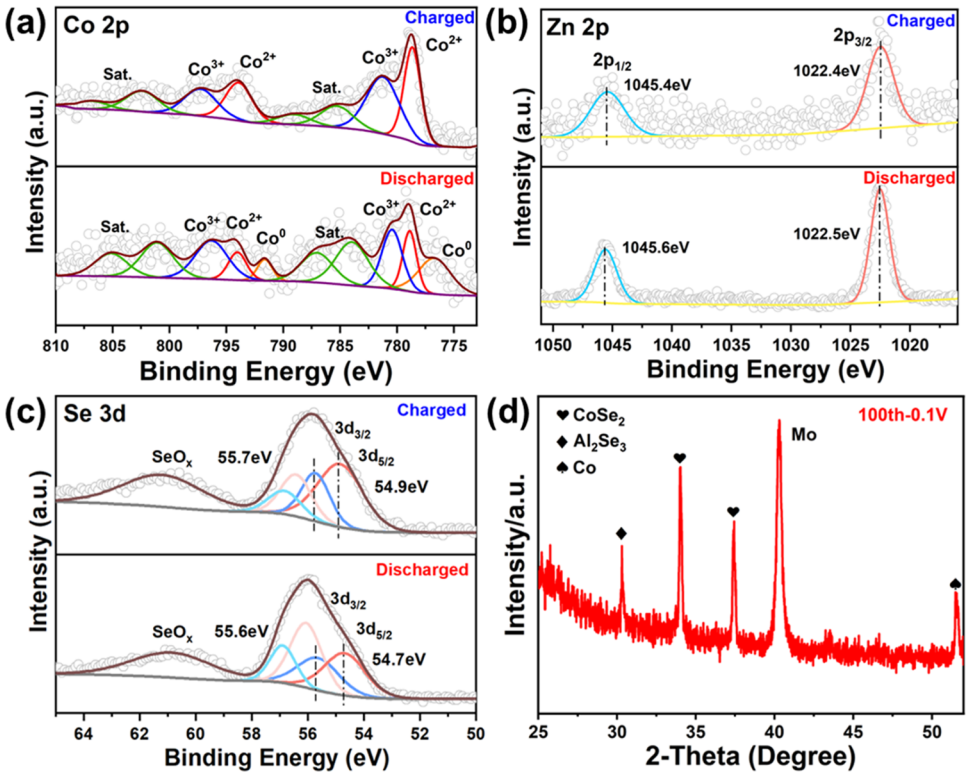

Figure 5. XPS spectra of (a) Co 2p, (b) Zn 2p, and (c) Se 3d for discharged and charged Co_3Se_4/ZnSe@C cathode after argon etching for 120 s. (d) *Ex situ* XRD patterns of Co_3Se_4/ZnSe@C electrode at fully discharged state after 100 cycles at 100 mA g^{-1}.

retained at 116.8 mA h g^{-1} after 500 cycles. The average capacity attenuation is 0.08% per cycle and the average Coulombic efficiency is 95%. The advantage of the Co_3Se_4/ZnSe heterostructure is clearly demonstrated by the performance comparison with the pure Co_3Se_4@C and ZnSe@C cathodes as displayed in Figure 3c. Representative discharge−charge curves of pure Co_3Se_4@C and ZnSe@C cathodes are shown in Figure S7. This observation is strong evidence that

https://doi.org/10.1021/acsami.2c23205
ACS Appl. Mater. Interfaces 2023, 15, 11906−11913

the capacity of the Co_3Se_4/ZnSe@C heterostructure is higher than the simple sum of that of pure Co_3Se_4@C and ZnSe@C. This synergistic improvement of specific capacity can be attributed to the facile conversion kinetics due to the high electron conductivity and Al^{3+} ion diffusion at the heterostructure interface between Co_3Se_4 and ZnSe, which also improves the rate capability of the Co_3Se_4/ZnSe@C heterostructure as demonstrated in Figure 3d. The TEM images and elemental mappings of the Co_3Se_4/ZnSe@C nanocubes after 100 cycles at 100 mA g^{-1} are displayed in Figure 3e. The nanocubes still maintain a stable hollow structure, and Co, Zn, Al, and Se elements are uniformly dispersed in the carbon framework, proving excellent structural stability.

To understand the facile kinetics of the conversion reaction of the Co_3Se_4/ZnSe@C cathode, the capacity contributions from the kinetics-limited and diffusion-limited processes were calculated from the cyclic voltammogram (CV) analysis. Figure 4a illustrates CV curves measured at different scanning rate from 1 to 5 mV s^{-1}, and the peak current (i) and scanning rate (v) conform to the following formula[19,32]

$$i = av^b \tag{2}$$

where a is a scaling factor and b is the exponent, the value of which is conventionally used to characterize the kinetics of the electrochemical reactions. If the reaction rate is controlled by the diffusion of ions in solid-state electrode materials, b is equal to 0.5. If the reaction rate is controlled by the intrinsic kinetics of the reaction, b is equal to 1. A b value between 0.5 and 1 suggests a mixed reaction kinetics. The b value derived from the log plot of i versus v in Figure 4b is 0.858 for reduction and 0.857 for oxidation, both of which are in excellent agreement with each other and indicate that the redox of Co_3Se_4/ZnSe@C is largely controlled by the intrinsic kinetics not by the Al^{3+} ion diffusion. Under the same experimental condition, the b values of pure Co_3Se_4@C with a similar surface area (surface area analysis in Figure S8) are 0.775 for reduction and 0.764 for oxidation as shown in Figure 4d. The pure sample without heterostructure shows inferior reaction kinetics, further proving that the heterostructure promotes fast ion diffusion and reaction kinetics.

To understand the conversion mechanism of the Co_3Se_4/ZnSe@C in the electrochemical reaction with Al, the chemical state of the electrode after full discharge and charge at 100 mA g^{-1} was analyzed with XPS. Figure 5a shows the Co 2p XPS spectra after the electrode reaction, the spectrum at a fully discharged state shows a relatively lower Co^{2+} peak intensity compared to the original state, which suggests that Co is reduced during discharge. The Co 2p spectrum at a fully charged state indicates that the relative intensity of the Co^{2+} peak increases, but is not back to the initial state. This observation indicates that the redox reaction of Co^{2+}/Co^0 is involved in the discharge−charge of Co_3Se_4/ZnSe@C. On the other hand, Figure 5b indicates that the Zn 2p spectra at fully discharged/charged states are identical to that at the original state. Therefore, Zn is inactive during the electrochemical process. The Se 3d spectrum at a fully discharged state in Figure 5c indicates relatively lowered Se^{2-} peaks at 55.6 eV ($3d_{3/2}$) and 54.7 eV ($3d_{5/2}$) and enhanced peaks at higher binding energy, which is due to the formation of diselenide (Se_2^{2-}). After the charging process, the intensity of Se 3d peaks index as Se^{2-} was increased, indicating a reversible reaction.

The conversion mechanism of Co_3Se_4/ZnSe@C was further verified with the *ex situ* XRD pattern of the long-cycled heterostructure electrode shown in Figure 5d. When discharged to 0.1 V after the 100th cycle, the presence of $CoSe_2$, elemental Co, and Al_2Se_3 was detected, confirming the conversion mechanism from Co_3Se_4 to $CoSe_2$ during discharging, which is also consistent with the Co 2p XPS spectrum. According to the XRD and XPS results, a possible discharge−charge reaction of the Co_3Se_4/ZnSe@C heterostructure is proposed as follows.

$$Co_3Se_4 + \frac{4}{3}Al^{3+} + 4e^- \leftrightarrow CoSe_2 + \frac{2}{3}Al_2Se_3 + 2Co \tag{3}$$

CONCLUSION

We demonstrate that the kinetics of the electrochemical conversion can be enhanced by creating a heterostructure between two transition-metal selenides. The theoretical and experimental results both indicate that the internal electric field generated by the heterostructure reduces the diffusion barrier of Al^{3+} and optimizes the electron transfer. Therefore, the designed Co_3Se_4/ZnSe@C electrode material demonstrates improve specific capacity and cycle stability compared to single-phase selenides. This innovative strategy to construct a heterostructure interface can be used to develop electrode materials to improve battery reaction kinetics.

ASSOCIATED CONTENT

Supporting Information

The Supporting Information is available free of charge at https://pubs.acs.org/doi/10.1021/acsami.2c23205.

SEM images of ZIF-67 nanotubes; TEM images and elemental mapping of ZIF-67/ZIF-8, hollow-ZIF-67/ZIF-8, hollow-Co/Zn, Co@C, Co_3Se_4@C, Zn@C, and ZnSe@C nanoparticles; thermogravimetric analysis curves of Co_3Se_4/ZnSe@C, Co_3Se_4@C, and ZnSe@C nanoparticles; galvanostatic discharge−charge curves of Co_3Se_4@C and ZnSe@C; N_2 adsorption−desorption isotherms of Co_3Se_4/ZnSe@C, Co_3Se_4@C, and ZnSe@C nanoparticles (PDF)

AUTHOR INFORMATION

Corresponding Authors

Guocheng Lv − *Engineering Research Center of Ministry of Education for Geological Carbon Storage and Low Carbon Utilization of Resources, Beijing Key Laboratory of Materials Utilization of Nonmetallic Minerals and Solid Wastes, National Laboratory of Mineral Materials, School of Materials Science and Technology, China University of Geosciences, Beijing 100083, China*; orcid.org/0000-0002-3719-8431; Email: guochenglv@cugb.edu.cn

Changchun Zhao − *School of Science, China University of Geosciences, Beijing 100083, China*; Email: zhaocc@cugb.edu.cn

Juchen Guo − *Department of Chemical and Environmental Engineering, University of California, Riverside, California 92521, United States; Materials Science and Engineering Program, University of California, Riverside, California 92521, United States*; orcid.org/0000-0001-9829-1202; Email: jguo@engr.ucr.edu

Authors

Tianming Liu − *School of Science, China University of Geosciences, Beijing 100083, China*

Meng Liu − *Engineering Research Center of Ministry of Education for Geological Carbon Storage and Low Carbon Utilization of Resources, Beijing Key Laboratory of Materials Utilization of Nonmetallic Minerals and Solid Wastes, National Laboratory of Mineral Materials, School of Materials Science and Technology, China University of Geosciences, Beijing 100083, China*

Libing Liao − *Engineering Research Center of Ministry of Education for Geological Carbon Storage and Low Carbon Utilization of Resources, Beijing Key Laboratory of Materials Utilization of Nonmetallic Minerals and Solid Wastes, National Laboratory of Mineral Materials, School of Materials Science and Technology, China University of Geosciences, Beijing 100083, China*

Hao Liu − *School of Science, China University of Geosciences, Beijing 100083, China*

Jiayan Shi − *Department of Chemical and Environmental Engineering, University of California, Riverside, California 92521, United States*

Jian Zhang − *Materials Science and Engineering Program, University of California, Riverside, California 92521, United States;* orcid.org/0000-0003-0356-7611

Complete contact information is available at: https://pubs.acs.org/10.1021/acsami.2c23205

Notes

The authors declare no competing financial interest.

■ ACKNOWLEDGMENTS

This work was supported by the National Natural Science Foundation of China (No. 21875223). J.S., J.Z., and J.G. acknowledge the support from U.S. National Science Foundation through grant CBET-1751929.

■ REFERENCES

(1) Zhang, Y.; Liu, S.; Ji, Y.; Ma, J.; Yu, H. Emerging Nonaqueous Aluminum-Ion Batteries: Challenges, Status, and Perspectives. *Adv. Mater.* **2018**, *30*, No. e1706310.

(2) Wu, F.; Yang, H.; Bai, Y.; Wu, C. Paving the Path toward Reliable Cathode Materials for Aluminum-Ion Batteries. *Adv. Mater.* **2019**, *31*, No. e1806510.

(3) Elia, G. A.; Marquardt, K.; Hoeppner, K.; Fantini, S.; Lin, R.; Knipping, E.; Peters, W.; Drillet, J. F.; Passerini, S.; Hahn, R. An Overview and Future Perspectives of Aluminum Batteries. *Adv. Mater.* **2016**, *28*, 7564−7579.

(4) Bitenc, J.; Košir, U.; Vizintin, A.; Lindahl, N.; Krajnc, A.; Pirnat, K.; Jerman, I.; Dominko, R. Electrochemical mechanism of Al metal−organic battery based on phenanthrenequinone. *Energy Mater. Adv.* **2021**, *2021*, No. 9793209.

(5) Gu, S.; Haoyi, Y.; Yuan, Y.; Gao, Y.; Zhu, N.; Wu, F.; Bai, Y.; Wu, C. Solvent Effects on Kinetics and Electrochemical Performances of Rechargeable Aluminum Batteries. *Energy Mater. Adv.* **2022**, *2022*, No. 9790472.

(6) Zhu, N.; Zhang, K.; Wu, F.; Bai, Y.; Wu, C. Ionic liquid-based electrolytes for aluminum/magnesium/sodium-ion batteries. *Energy Mater. Adv.* **2021**, *2021*, No. 9204217.

(7) Yang, H.; Li, H.; Li, J.; Sun, Z.; He, K.; Cheng, H. M.; Li, F. The Rechargeable Aluminum Battery: Opportunities and Challenges. *Angew. Chem., Int., Ed.* **2019**, *58*, 11978−11996.

(8) Faegh, E.; Ng, B.; Hayman, D.; Mustain, W. E. Practical assessment of the performance of aluminium battery technologies. *Nat. Energy* **2021**, *6*, 21−29.

(9) Canepa, P.; Sai Gautam, G.; Hannah, D. C.; Malik, R.; Liu, M.; Gallagher, K. G.; Persson, K. A.; Ceder, G. Odyssey of Multivalent Cathode Materials: Open Questions and Future Challenges. *Chem. Rev.* **2017**, *117*, 4287−4341.

(10) Lin, Z.; Mao, M.; Yang, C.; Tong, Y.; Li, Q.; Yue, J.; Yang, G.; Zhang, Q.; Hong, L.; Yu, X.; et al. Amorphous anion-rich titanium polysulfides for aluminum-ion batteries. *Sci. Adv.* **2021**, *7*, No. eabg6314.

(11) Ng, K. L.; Amrithraj, B.; Azimi, G. Nonaqueous rechargeable aluminum batteries. *Joule* **2022**, *6*, 134−170.

(12) Geng, L.; Lv, G.; Xing, X.; Guo, J. Reversible Electrochemical Intercalation of Aluminum in Mo_6S_8. *Chem. Mater.* **2015**, *27*, 4926−4929.

(13) Geng, L.; Scheifers, J. P.; Zhang, J.; Bozhilov, K. N.; Fokwa, B. P. T.; Guo, J. Crystal Structure Transformation in Chevrel Phase Mo_6S_8 Induced by Aluminum Intercalation. *Chem. Mater.* **2018**, *30*, 8420−8425.

(14) Tong, Y.; Gao, A.; Zhang, Q.; Gao, T.; Yue, J.; Meng, F.; Gong, Y.; Xi, S.; Lin, Z.; Mao, M.; Peng, S.; Wang, X.; Xiao, D.; Su, D.; Luo, Y.; Li, H.; Chen, L.; Suo, L.; Gu, L. Cation-synergy stabilizing anion redox of Chevrel phase Mo_6S_8 in aluminum ion battery. *Energy Storage Mater.* **2021**, *37*, 87−93.

(15) Lee, B.; Lee, H. R.; Yim, T.; Kim, J. H.; Lee, J. G.; Chung, K. Y.; Cho, B. W.; Oh, S. H. Investigation on the Structural Evolutions during the Insertion of Aluminum Ions into Mo_6S_8 Chevrel Phase. *J. Electrochem. Soc.* **2016**, *163*, A1070−A1076.

(16) Mori, T.; Orikasa, Y.; Nakanishi, K.; Kezheng, C.; Hattori, M.; Ohta, T.; Uchimoto, Y. Discharge/charge reaction mechanisms of FeS_2 cathode material for aluminum rechargeable batteries at 55 °C. *J. Power Sources* **2016**, *313*, 9−14.

(17) Cai, T.; Zhao, L.; Hu, H.; Li, T.; Li, X.; Guo, S.; Li, Y.; Xue, Q.; Xing, W.; Yan, Z.; Wang, L. Stable $CoSe_2$/carbon nanodice@reduced graphene oxide composites for high-performance rechargeable aluminum-ion batteries. *Energy Environ. Sci.* **2018**, *11*, 2341−2347.

(18) Tu, J.; Wang, M.; Xiao, X.; Lei, H.; Jiao, S. Nickel Phosphide Nanosheets Supported on Reduced Graphene Oxide for Enhanced Aluminum-Ion Batteries. *ACS Sustainable Chem. Eng.* **2019**, *7*, 6004−6012.

(19) Li, C.; Dong, S.; Wang, P.; Wang, C.; Yin, L. Metal−Organic Frameworks-Derived Tunnel Structured $Co_3(PO_4)_2$@C as Cathode for New Generation High-Performance Al-Ion Batteries. *Adv. Energy Mater.* **2019**, *9*, No. 1902352.

(20) Hong, H.; Liu, J.; Huang, H.; Atangana Etogo, C.; Yang, X.; Guan, B.; Zhang, L. Ordered Macro-Microporous Metal-Organic Framework Single Crystals and Their Derivatives for Rechargeable Aluminum-Ion Batteries. *J. Am. Chem. Soc.* **2019**, *141*, 14764−14771.

(21) Yao, L.; Ju, S.; Xu, T.; Yu, X. Spatial Isolation-Inspired Ultrafine $CoSe_2$ for High-Energy Aluminum Batteries with Improved Rate Cyclability. *ACS Nano* **2021**, *15*, 13662.

(22) Yoo, D. J.; Heeney, M.; Glocklhofer, F.; Choi, J. W. Tetradiketone macrocycle for divalent aluminium ion batteries. *Nat. Commun.* **2021**, *12*, No. 2386.

(23) Liu, T.; Lv, G.; Liu, M.; Zhao, C.; Liao, L.; Liu, H.; Shi, J.; Zhang, J.; Guo, J. Cation-intercalation and conversion-type cathode materials for rechargeable aluminum batteries. *Mater. Chem. Front.* **2022**, *6*, 280−296.

(24) Zhuang, R.; Huang, Z.; Wang, S.; Qiao, J.; Wu, J.-C.; Yang, J. Binder-free cobalt sulfide@carbon nanofibers composite films as cathode for rechargeable aluminum-ion batteries. *Chem. Eng. J.* **2021**, *409*, No. 128235.

(25) Hu, Y.; Ye, D.; Luo, B.; Hu, H.; Zhu, X.; Wang, S.; Li, L.; Peng, S.; Wang, L. A Binder-Free and Free-Standing Cobalt Sulfide@Carbon Nanotube Cathode Material for Aluminum-Ion Batteries. *Adv. Mater.* **2018**, *30*, No. 1703824.

(26) Ma, X.; Chen, J.; Zhao, W. Construction of series-wound architectures composed of metal-organic framework-derived hetero-$(CoFe)Se_2$ hollow nanocubes confined into a flexible carbon skeleton as a durable sodium storage anode. *Nanoscale* **2020**, *12*, 22161−22172.

(27) Lin, Y.; Xu, Y.; Mayer, M. T.; Simpson, Z. I.; McMahon, G.; Zhou, S.; Wang, D. Growth of p-type hematite by atomic layer deposition and its utilization for improved solar water splitting. *J. Am. Chem. Soc.* **2012**, *134*, 5508−5511.
(28) Low, J.; Yu, J.; Jaroniec, M.; Wageh, S.; Al-Ghamdi, A. A. Heterojunction Photocatalysts. *Adv. Mater.* **2017**, *29*, No. 1601694.
(29) Ma, D.; Hu, B.; Wu, W.; Liu, X.; Zai, J.; Shu, C.; Tadesse Tsega, T.; Chen, L.; Qian, X.; Liu, T. L. Highly active nanostructured CoS_2/CoS heterojunction electrocatalysts for aqueous polysulfide/iodide redox flow batteries. *Nat. Commun.* **2019**, *10*, No. 3367.
(30) Zhou, W.; Cheng, C.; Liu, J.; Tay, Y. Y.; Jiang, J.; Jia, X.; Zhang, J.; Gong, H.; Hng, H. H.; Yu, T.; Fan, H. J. Epitaxial Growth of Branched α-Fe_2O_3/SnO_2 Nano-Heterostructures with Improved Lithium-Ion Battery Performance. *Adv. Funct. Mater.* **2011**, *21*, 2439−2445.
(31) Zheng, Y.; Zhou, T.; Zhang, C.; Mao, J.; Liu, H.; Guo, Z. Boosted Charge Transfer in SnS/SnO_2 Heterostructures: Toward High Rate Capability for Sodium-Ion Batteries. *Angew. Chem., Int. Ed.* **2016**, *55*, 3408−3413.
(32) Liu, P.; Han, J.; Zhu, K.; Dong, Z.; Jiao, L. Heterostructure $SnSe_2$/ZnSe@PDA Nanobox for Stable and Highly Efficient Sodium-Ion Storage *Adv. Energy Mater.* 202010 242000741 DOI: 10.1002/aenm.202000741.
(33) Xie, X.; Ao, Z.; Su, D.; Zhang, J.; Wang, G. MoS_2/Graphene Composite Anodes with Enhanced Performance for Sodium-Ion Batteries: The Role of the Two-Dimensional Heterointerface. *Adv. Funct. Mater.* **2015**, *25*, 1393−1403.
(34) Shan, H.; Qin, J.; Ding, Y.; Sari, H. M. K.; Song, X.; Liu, W.; Hao, Y.; Wang, J.; Xie, C.; Zhang, J.; Li, X. Controllable Heterojunctions with a Semicoherent Phase Boundary Boosting the Potassium Storage of $CoSe_2$/$FeSe_2$. *Adv. Mater.* **2021**, *33*, No. e2102471.
(35) Li, Y.; Zhang, J.; Chen, Q.; Xia, X.; Chen, M. Emerging of Heterostructure Materials in Energy Storage: A Review. *Adv. Mater.* **2021**, *33*, No. e2100855.
(36) Xiao, S.; Li, X.; Zhang, W.; Xiang, Y.; Li, T.; Niu, X.; Chen, J. S.; Yan, Q. Bilateral Interfaces in In_2Se_3-$CoIn_2$-$CoSe_2$ Heterostructures for High-Rate Reversible Sodium Storage. *ACS Nano* **2021**, *15*, 13307.
(37) Wang, Y.; Kang, W.; Cao, D.; Zhang, M.; Kang, Z.; Xiao, Z.; Wang, R.; Sun, D. A yolk−shelled Co_9S_8/MoS_2−CN nanocomposite derived from a metal−organic framework as a high performance anode for sodium ion batteries. *J. Mater. Chem. A* **2018**, *6*, 4776−4782.
(38) Huang, S.; Wang, Z.; Von Lim, Y.; Wang, Y.; Li, Y.; Zhang, D.; Yang, H. Y. Recent Advances in Heterostructure Engineering for Lithium−Sulfur Batteries. *Adv. Energy Mater.* **2021**, *11*, No. 2003689.
(39) Hu, M.; Ju, Y.; Liang, K.; Suma, T.; Cui, J.; Caruso, F. Void Engineering in Metal-Organic Frameworks via Synergistic Etching and Surface Functionalization. *Adv. Funct. Mater.* **2016**, *26*, 5827−5834.
(40) Huang, Y.; Fang, Y.; Lu, X. F.; Luan, D.; Lou, X. W. D. Co_3O_4 Hollow Nanoparticles Embedded in Mesoporous Walls of Carbon Nanoboxes for Efficient Lithium Storage. *Angew. Chem., Int. Ed.* **2020**, *59*, 19914−19918.
(41) Yin, Y.; Rioux Robert, M.; Erdonmez Can, K.; Hughes, S.; Somorjai Gabor, A.; Alivisatos, A. P. Formation of Hollow Nanocrystals Through the Nanoscale Kirkendall Effect. *Science* **2004**, *304*, 711−714.
(42) Feng, J.; Yin, Y. Self-Templating Approaches to Hollow Nanostructures. *Adv. Mater.* **2019**, *31*, No. e1802349.
(43) Li, H.; Qian, X.; Xu, C.; Huang, S.; Zhu, C.; Jiang, X.; Shao, L.; Hou, L. Hierarchical Porous Co9S8/Nitrogen-Doped Carbon@MoS2 Polyhedrons as pH Universal Electrocatalysts for Highly Efficient Hydrogen Evolution Reaction. *ACS Appl. Mater. Interfaces* **2017**, *9*, 28394−28405.
(44) Bai, J.; Meng, T.; Guo, D.; Wang, S.; Mao, B.; Cao, M. Co_9S_8@MoS_2 core−shell heterostructures as trifunctional electrocatalysts for overall water splitting and Zn−air batteries. *ACS Appl. Mater. Interfaces* **2018**, *10*, 1678−1689.
(45) Ai, L.; Su, J.; Wang, M.; Jiang, J. Bamboo-structured nitrogen-doped carbon nanotube coencapsulating cobalt and molybdenum carbide nanoparticles: An efficient bifunctional electrocatalyst for overall water splitting. *ACS Sustainable Chem. Eng.* **2018**, *6*, 9912−9920.
(46) Fall, C. J.; Binggeli, N.; Baldereschi, A. Deriving accurate work functions from thin-slab calculations. *J. Phys.: Condens. Matter* **1999**, *11*, 2689.
(47) Zheng, J.; Bock, D. C.; Tang, T.; Zhao, Q.; Yin, J.; Tallman, K. R.; Wheeler, G.; Liu, X.; Deng, Y.; Jin, S.; Marschilok, A. C.; Takeuchi, E. S.; Takeuchi, K. J.; Archer, L. A. Regulating electrodeposition morphology in high-capacity aluminium and zinc battery anodes using interfacial metal−substrate bonding. *Nat. Energy* **2021**, *6*, 398−406.
(48) Long, Y.; Li, H.; Ye, M.; Chen, Z.; Wang, Z.; Tao, Y.; Weng, Z.; Qiao, S.-Z.; Yang, Q.-H. Suppressing Al dendrite growth towards a long-life Al-metal battery. *Energy Storage Mater.* **2021**, *34*, 194−202.